ADVANCED FUNCTIONAL MATERIALS
www.afm-journal.de

Active-Matrix Sensing Array Assisted with Machine-Learning Approach for Lumbar Degenerative Disease Diagnosis and Postoperative Assessment

Di Liu, Dongli Zhang, Zhuoran Sun, Siyu Zhou, Wei Li, Chengyu Li, Weishi Li, Wei Tang,* and Zhong Lin Wang**

Lumbar degenerative disease (LDD) refers to the nerve compression syndrome such as neurogenic intermittent claudication and lower limb pain, which disturbs people's daily life, and its incidence increases with age. Traditional diagnosis often employs magnetic response imaging or other imaging examinations. But the radiological data have uncertain clinical correlation and often be overemphasized in clinical decision making. Here, an active-matrix sensing array (AMSA) is proposed to measure plantar pressure during walking, in order to improve LDD diagnostic processes. An array of piezoelectric sensors with high robustness are assembled. Combined with a support vector machine (SVM) supervised learning algorithm, the system can classify the common human motions of half-squat, squat, jump, walk and jog with an accuracy up to 99.2%, demonstrating its capability of recognizing personal activities. More importantly, in 62 clinical samples of lumbar degenerative patients, the system can perform an artificial intelligence diagnosis, achieving an accuracy of 100% with an area under receiver operating characteristic curve of 0.998, and also gives out recovery assessments after surgery. Since the personal plantar pressure is also indicative of other diseases, such as diabetes and fasciitis, the system can be extended to other medical aspects, showing a broad impact in biomedical engineering.

1. Introduction

Lumbar degenerative disease (LDD) refers to the nerve compression syndrome, in which the lumbar canal narrows and compresses the dural sac, cauda equian, or nerve root.[1,2] It usually leads to pain or numbness and weakness in the lower back,[3] buttocks, and different degrees of neurogenic intermittent claudication (NIC), which limits patients' daily activities and labor capacity.[4] As the incidence of LDD increases with age, it is about 9.3% in the general population and up to 47% in individuals older than 60 years.[5] Clinical diagnosis now relies on magnetic resonance imagining (MRI), X-ray imagining, or other imaging examinations,[6] which are able to present the shape of the lumbar spinal canal. But the radiological data have uncertain clinical correlation and often be overemphasized in clinical decision making.[7] Therefore, clinical

D. Liu, D. Zhang, C. Li, W. Tang, Z. L. Wang
CAS Center for Excellence in Nanoscience
Beijing Institute of Nanoenergy and Nanosystems
Chinese Academy of Sciences
Beijing 100083, China
E-mail: puh3liweishi@bjmu.edu.cn, puh3liweishi@163.com; tangwei@binn.cas.cn; zlwang@binn.cas.cn

D. Liu, C. Li, W. Tang, Z. L. Wang
School of Nanoscience and Technology
University of Chinese Academy of Sciences
Beijing 100049, China

D. Zhang
Center on Nanoenergy Research
School of Physical Science & Technology
Guangxi University
Nanning 530004, China

Z. Sun, S. Zhou, W. Li, W. Li
Department of Orthopaedics
Peking University Third Hospital
No. 49 North Garden Road, Haidian District, Beijing 100191, China

Z. Sun, S. Zhou, W. Li, W. Li
Engineering Research Center of Bone and Joint Precision Medicine
Ministry of Education
No. 49 North Garden Road, Haidian District, Beijing 100191, China

Z. Sun, S. Zhou, W. Li, W. Li
Beijing Key Laboratory of Spinal Disease Research
No. 49 North Garden Road, Haidian District, Beijing 100191, China

W. Tang
Institute of Applied Nanotechnology
Jiaxing, Zhejiang 314031, P. R. China

Z. L. Wang
CUSPEA Institute of Technology
Wenzhou, Zhejiang 325024, China

Z. L. Wang
School of Materials Science and Engineering
Georgia Institute of Technology
Atlanta, GA 30332-0245, USA

The ORCID identification number(s) for the author(s) of this article can be found under https://doi.org/10.1002/adfm.202113008.

DOI: 10.1002/adfm.202113008

diagnosis strongly depends on the physical examination which was mainly decided by medical's experience.[8]

Recent studies show that the gait of patients with LDD is different from that of normal people.[9] Evaluation parameters include walking speed, swing time, single supporting time, and so on,[10] by means of bulky instruments, for example, walkway system,[11] cameras.[12] The wearable accelerometer is proposed to perform activity monitoring, but without subtle gait information.[13] Lord[14] and James[15] preliminarily discovered that patients' plantar pressure is related to LDD,[16] which attract researchers to attempt to design portable devices for assisting LDD diagnosis and recovery based on plantar pressure.[17–21] A pressure platform is presented as an additional diagnostic method for LDD and able to indicate the effectiveness of operative treatment and physical therapy after surgery.[22] While, in-shoe systems[23–26] are definitely preferable due to the convenience and capability of reflecting the interface between the foot and the shoe. However, the drawback is that the spatial resolution of the data is low due to fewer sensors. Additionally, personal gaits refer to complex time-varying spatial plantar pressure change. Several formalistic parameters are insufficient and sometimes misleading for evaluating patients' symptoms. Therefore, more comprehensive analysis approaches are in demand, such as machine learning.[27,28]

Here, we designed a wearable in-shoe monitoring system comprising a flexible insole with active-matrix sensing spots (more than 30), and a data-processing circuit board. A cell-phone application program (APP) is also developed to real-time record and display the wearers' plantar pressure. Furthermore, a support vector machine (SVM) supervised learning algorithm is employed for artificial intelligent (AI) recognition. Compared with previous apparatus, the advances presented here involves: 1) real-time plantar pressure mapping by active-matrix sensing array (AMSA); 2) the employed SVM machine-learning algorithm exhibiting an over 99.2% accuracy for recognizing human motions, including squat, half-squat, jump, walk and jog; 3) clinical experiments demonstrated that the combined system shows an LDD diagnostic ability with a recognizing accuracy 100%, as well as recovery state assessment capability. We anticipate that, as the patient's medical database gets larger, the present system could be more significant in assisting doctors to make quantitative diagnosis, and further gradually gives rise to AI medical consulting; furthermore, since personal plantar pressure is also indicative for other diseases, such as diabetes and fasciitis, the system can be extended to other medical aspects, showing a board impact in biomedical engineering.

2. Results

2.1. The Monitoring System

Wearable, portable and intelligent systems exhibit great significance in data collection,[29–31] behavioral analysis,[32,33] and health monitoring.[34] Here, an AMSA is presented to assist doctor in making diagnosis of LDD and giving recovery assessments (**Figure 1**). The AMSA is composed of a flexible printed circuit board (FPCB) with a 100-µm-thick polyimide as the substrate and

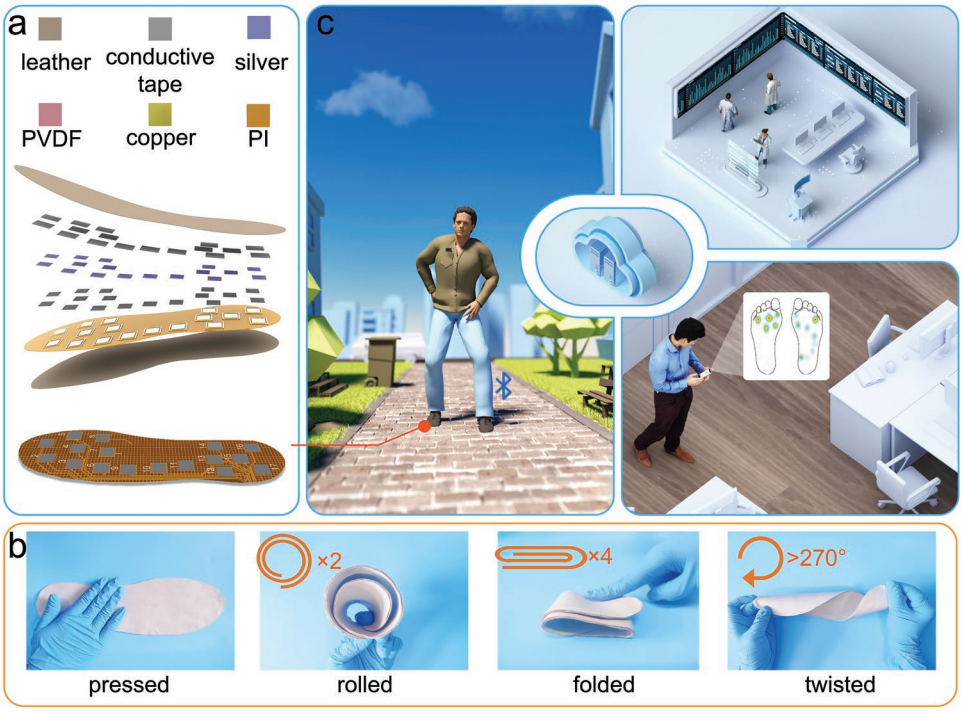

Figure 1. The design of AMSA for LDD diagnosis and recovery assessment. a) Exploded overall structure of AMSA comprising of FPCB, piezoelectric film, conductive tape, and leather. b) Photograph illustrates the flexibility of AMSA that can be pressed, rolled, folded, and twisted. c) Typical scene of sensing LDD patient's or normal people's plantar pressure with AMSA when walking. The data are transmitted to portable cell phone and even uploaded onto the medical cloud server which can be assessed by a doctor for illness evaluation and recovery assessment.

an array of pressure-sensitive spots made up of polyvinylidene fluoride (PVDF) possessing the piezoelectric characteristic[35] (Figure 1a). The PVDF has its top and bottom surfaces both covered by silver. And then two conductive tapes are utilized to fix and electrically connect the PVDF piece to the FPCB. Finally, the as-fabricated sensing matrix is encapsulated with leather (sheepskin), forming a shape of an insole and a total thickness of 1.3 mm. The fabrication and parameters in detail can be found in Experimental Section, Figure S1, Supporting Information.

Due to the flexibility of the above materials, the whole AMSA can be pressed, rolled, folded, and twisted with high adaptivity (Figure 1b), making it comforting to serve as an insole. Moreover, the AMSA can sense the real-time plantar pressure variation and transmit the data through a follow-up circuit based on Bluetooth (Figures S2 and S3, Supporting Information). The small circuit module is placed near the ankle, embedded in a wristband (Figure S3d, Supporting Information). A cellphone with the customized APP can display the plantar pressure mapping, as well as specific pressure curve of each spot (Figure S4, Supporting Information). Furthermore, the data can be uploaded onto the medical cloud server, which can be accessed by patients' doctors for illness evaluation or recovery assessment in the future (Figure 1c).

2.2. Characterization of AMSA

Figure 2a shows that the AMSA is composed of 17 PVDF sensors, as well as the follow-up circuit. The sensors array is marked in order, from the toe to the heel. As for the circuit, the amplifier can filter out noise benefitted by the feedback resistor and capacitor constituting a lowpass filter. The value of the resistor and capacitor, as well as the working principle and the passband's calculation of amplifying circuit can be found in Experimental Section and Note S1, Supporting Information. Finally, the processed voltage will be transmitted to the cell phone through Bluetooth in real-time. Figure 2b,c illustrates the output voltages tested under different pressure (0 to around 200 kPa) without/with amplifier, respectively. Both show excellent linear relationship between the output voltage and the pressure, with slops of 0.007 and 0.016, respectively. And the output with the amplifier shows a higher drive capability. The test condition can be found in Figure S5, Supporting Information. The durability of the PVDF sensor was tested under 5000, 7000, and 10 000 press cycles with 300 kPa then the output was measured under the pressure of 165 kPa (Figure 2d), which shows quite a stability. More test results with enormous press cycles are illustrated in Figure S5d, Supporting Information. Figure 2e shows an enlarged view of the output voltage, showing a response time of 100 ms and a recovery time of 80 ms. Additionally, the temperature and humidity influences on the output performance of the sensor were examined in the previous studies.[36,37] In our experiment, the leather was employed to encapsulate the sensor and thus improve the anti-interference ability. It can be found in Figure 2f that, the output voltage is around 1.8 V with a variation of about 4.6% when the humidity changes from 42% to 85%. And when the temperature varies from 23.9 to 43 degrees Celsius (Figure 2g), the voltage variation is about 7.3%. The anti-interference ability has a significant improvement compared with the voltage variations around 30% and 20% in previous study.[36] Finally, a typical real-time pressure change detected by the AMSA during one-step move is presented in Figure 2h and more sensing data can be found in Figures S6 and S7, Supporting Information. The curves from top to bottom represent the sensing data from the toe to the heel, respectively. The dash line indicates that the signal begins from the heel to the toe successively, with the high-voltage area appearing at the heel and the forefoot area. It matches well with the ergonomics during walking, indicating the AMSA's capability of human plantar pressure sensing.

2.3. Human Motion Classification by AMSA

Subsequently, we employed the AMSA to classify five common human motions: half-squat, squat, jump, walk and jog (**Figure 3**). The plantar pressure distributions are obviously different as shown in Figure 3a, which illustrates the real-time output voltages of the AMSA in 5 s. Figure 3b shows the voltage from diverse foot areas in detail. The dense and the magnitude of signals indicate the intensity and frequency of motions, which can be used to classify different motions. For example, the peak values of squat and half-squat are lower than others because these two motions move slowly, leading to lower pressure on the AMSA. The voltage of half-squat and squat is about 1.15 V, appearing at heel and forefoot areas, when the participant stands up or squats down. Moreover, the pressure distribution of squat is similar to that of half-squat, except a higher voltage due to a higher downward motion. An instantaneous peak value occurs at the moment of jump and the force location is at the forefoot area. As for walk and jog motions, almost all sensors have outputs, but the frequency of jog is apparently higher than walk.

Considering the multidimensional and enormous data, an SVM machine-learning algorithm is designed to classify the above motions. Figure 3c illustrates the schematic of machine-learning framework, including data collection, eigenvalues extraction, data processing, model training, and prediction. Here, we extracted the average voltage value as the eigenvalue to train the machine-learning model (Figure S8a–e, Supporting Information). A total of 45 samples of each motion are obtained and the data collection can be found in Experimental Section. 38 samples of them are used as model training data set while the other 7 are selected as the prediction data set. After eigenvalue extraction, the eigenvalues are pre-processed such as filtered or normalized to optimize the training process (Figure S8f, Supporting Information). The confusion matrix of trained model with fivefold cross-validation shows the precision of nearly 100%. There was only one erroneous judgment that judged walk motion as jump (Figure 3d). Afterwards, the confusion matrix of prediction illustrated that all the other 5 motions were predicted right (Figure 3e), which demonstrates the feasibility of the machine-learning-assisted active-matrix sensing array (MAS) in sensing and classifying human motions.

2.4. The LDD Diagnosis and Recovery Assessment by MAS

Since the MAS exhibits great effectiveness in recognizing human motions, and the symptom of LDD has a strong

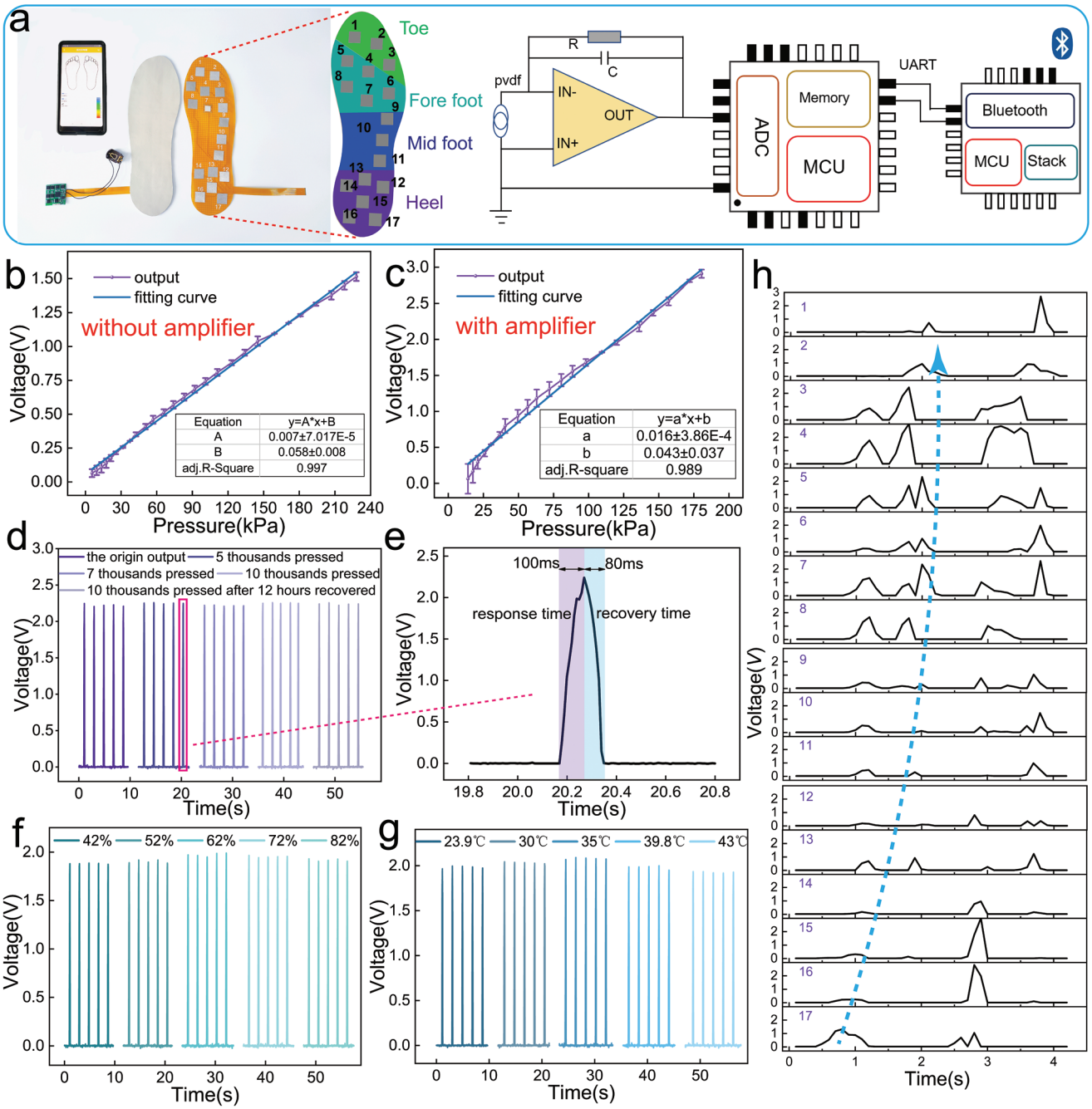

Figure 2. Characterization of the AMSA. a) The photograph of AMSA, as well as the customized APP with the schematic follow-up circuit shown on the right hand. b,c) The schematic of linear relationship between the output voltage and the pressure without amplifying circuit (b) or with amplifying circuit (c). d) The durability test of pressure sensor suffering from 5000, 7000, and 10 000 press under a force of 30 N. Then the output voltage of sensor was tested under a pressure of 165 kPa. e) An enlarged view of sensor's output voltage illustrating the response time 100 ms and recovery time 80ms. f,g) The output performance of pressure sensor under various humidity (f) and temperature (g) with testing force of 17.5 N. h) Illustration of a typical real-time pressure change detected by the AMSA during one-step move. The direction of the dotted line shows the signal begins from heel to toe.

relationship with the plantar pressure,[14–16] we utilized the MAS to investigate the LDD patients for establishing an assisting tool for helping doctors make diagnosis or assessing patients' recovery. 72 samples from patients and 73 samples from normal people (Experimental Section and Table S1, Supporting Information) are selected as model training data set (62 samples of patients and 63 samples of normal people) and prediction data set (10 samples of patients and 10 samples of normal people).

Figure 4a,b shows the X-Ray and MRI images of two typical cases of LDD. One is lumbar scoliosis, and the other is lumbar stenosis. The bent/narrow neural canal often causes the nerve compression, and leads to pain, numbness, or weakness in the lower back and buttocks, resulting in abnormal

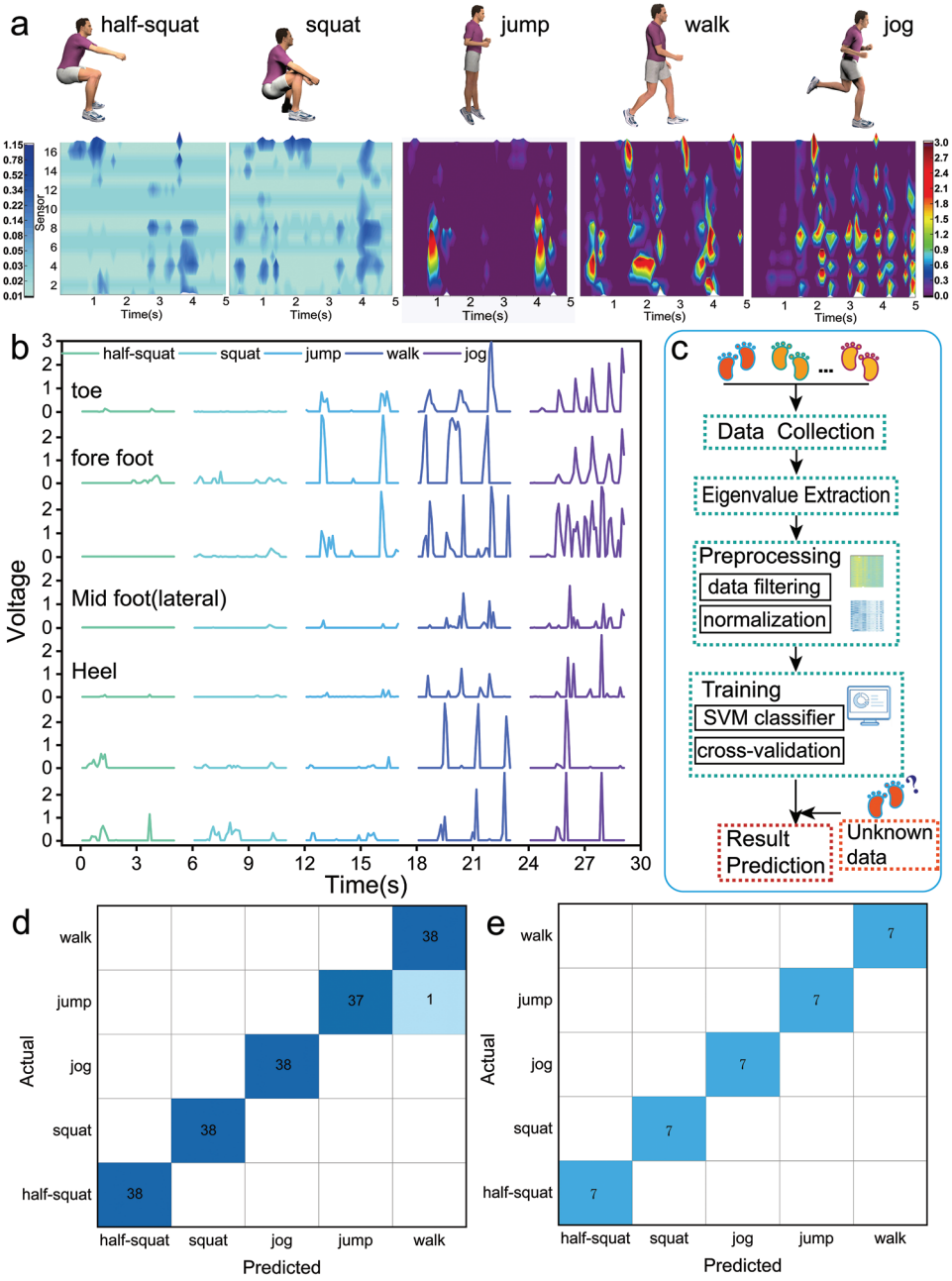

Figure 3. The capability of AMSA in detecting and classifying different human motions combined with machine-learning method. a) The plantar pressure distribution of five human motions (half-squat, squat, jump, walk, and jog) detected by AMSA. b) The excerpts of output voltage of toe, forefoot, midfoot, and heel corresponding to the five motions. c) The block diagram that demonstrates the procedure of the machine-learning model training. d,e) Confusion matrices exhibiting the result of trained model (d) with fivefold cross-validation and prediction (e).

plantar pressure during walking, compared to the normal person. Figure 4c,d presents the average and variance values as the eigenvalues of training data for two cases, respectively. And the great difference of plantar pressure between patients (upper photograph) and normal people (lower photograph) can be found. For instance, as shown in Figure 4c, the patient with lumbar scoliosis (marked with the blue block) shows an extremely large average value at sensor 4, located at the forefoot, compared with the normal people. That implies the pressure on his heel should be lower, corresponding with the results presented. Similar cases can also be found in Figure 4c, such as sample Nos. 7 and 15. However, the patient with lumbar stenosis (marked with the red block in Figure 4c) might possess a similar average pressure with the normal people, but the pressure variance shows different, as illustrated in Figure 4d. Most of the patient's pressure variances are higher than normal especially at sensor 4 to 8 (forefoot area) and sensor 16 (heel area). Thus, the enhanced machine-learning method (SVM) with two kinds of eigenvalues was used to analyze the relationship between the AMSA data and the LDD symptoms (Figure S9, Supporting Information). Based on the distribution in multidimensional space, the SVM can separate the patients

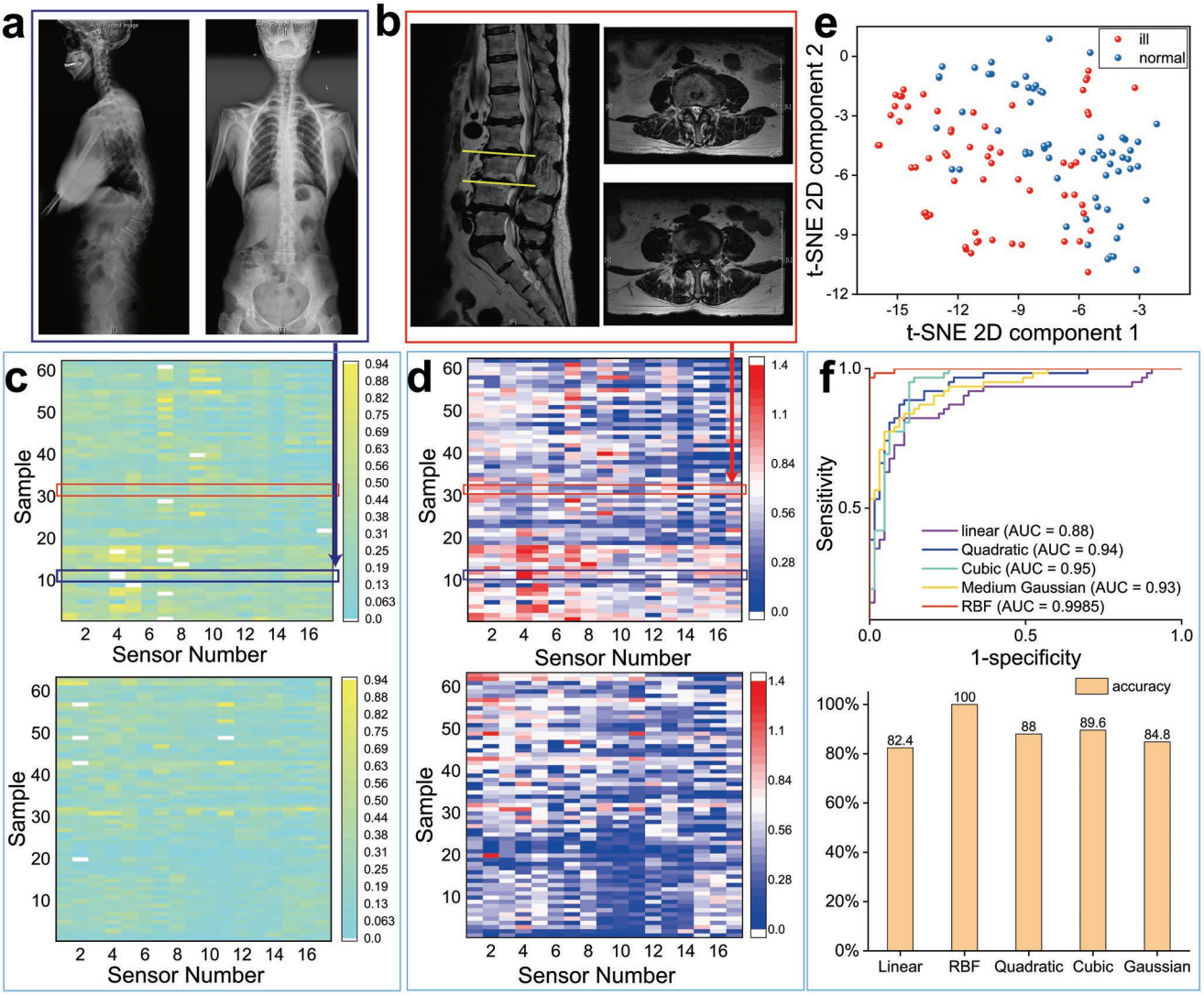

Figure 4. Preparation of machine-learning model training for the distinction of LDD. a,b) Two typical cases of LDD: lumbar scoliosis based on X-Ray (a) diagnosis and lumbar stenosis based on MRI (b) diagnosis. c,d) The average value (c) and variance value (d) of patients (upper part of the figure) and normal people (lower part of the figure) extracted as eigenvalue for training the machine-learning model. e) t-SNE analysis of the classification between patients and normal people based on average and variance eigenvalues presenting a definite difference. f) The ROC curve and accuracy of SVM model with different kernel functions showing the best RBF kernel function with AUC 0.998 and accuracy 100%.

from normal people. As shown in Figure 4e, the t-SNE analysis shows the definite difference between the ill and the normal in dimensionality reduction space.[38] Afterwards, different kernel functions[39] of SVM algorithm were employed to train the classification model and the results are summarized in Figure 4f and **Table 1**. According to the accuracy and receiver operating characteristic (ROC) curve, the SVM algorithm with RBF kernel achieves an accuracy of 100% and area under curve (AUC) value of 0.998 in distinguishing patients and the normal people, whereas the other kernels' accuracies are found to be below 90%, and the AUC values are below 0.94. The details of the performance evaluation of SVM with different kernel

Table 1. Performance evaluation of different SVM kennels for the prediction of LDD.

SVM kernel	AUC	Sn [%]	Sp [%]	Acc [%]	Mcc	PPV [%]	NPV [%]
Linear	0.88	0.76	0.89	0.824	0.65	0.87	0.79
Quadratic	0.94	0.85	0.90	0.88	0.76	0.90	0.86
Cubic	0.95	0.92	0.87	0.896	0.79	0.88	0.92
Gaussian	0.93	0.84	0.86	0.848	0.70	0.85	0.84
RBF	0.998	1	1	1	1	1	1

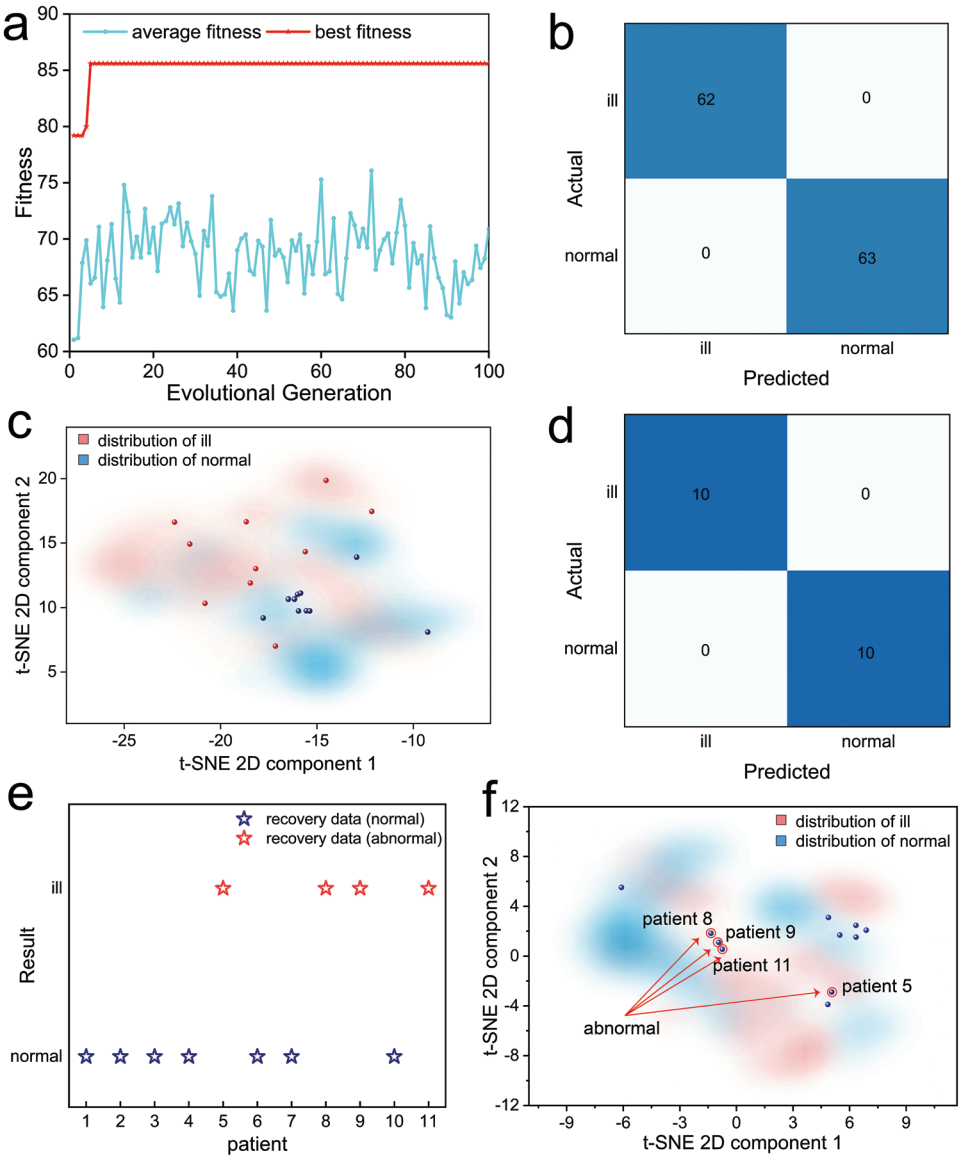

Figure 5. The LDD diagnosis and recovery assessment by MAS. a) Optimizing the key parameters C and G for SVM algorithm by maximizing the value of fitness function. b) The confusion matrix of the trained model under fivefold cross-validation. c) t-SNE analysis of the classification of patients and normal people. The areas are the distribution of LDD and normal people according to the trained data, and the scattered data of LDD and normal people distribute to the right area. d) The confusion matrix of the final predictive versus ground-truth outcomes showing the accuracy of 100%. e) The result of recovery assessment via MAS, and the prediction results of ill are proved to be not totally recovered. f) t-SNE analysis of the distribution of recovery data and trained model, which shows the samples predicted ill distributed at the boundary of ill and normal area.

functions are shown in Table 1, Figures S10 and S11, Supporting Information.

Accordingly, we selected radial basis function (RBF) kernel function for it exhibiting the best AUC and Matthews correlation coefficient (MCC) (Figure 4f and Table 1). C and G are the key parameters related to the classification performance of SVM.[40] After 100-times evolutional generations by Particle Swarm Optimization (PSO) algorithm,[41] the fitness function reaches its best value of 85.6% and the average fitness value is higher than 70%, obtaining the optimized C of 30.8968 and G of 1.6474, respectively (**Figure 5**a). The confusion matrix indicates that all 62 ill samples and all 63 normal samples were predicted right (Figure 5b). In addition, a predicted dataset consisting of 10 ill samples and 10 normal samples is used to verify the machine-learning model. The t-SNE illustrated that all the samples are classified in the right region (Figure 5c) and the confusion matrix in Figure 5d presented all samples classified correctly.

Furthermore, we utilized the MAS to examine the postoperative patient. The recognition results are plotted in Figure 5e, which indicates subjects Nos. 5, 8, 9, and 11 are unrecovered to some certain. Correspondingly, it is found that No. 5 felt pain in the left lower limb after taking surgery, No. 9 and 11 subjects felt numb to some degree, and No. 11 subject with a high Oswestry Disability Index (ODI)[42] felt tiny unnatural (medical diagnosis in Figure S12 and Table S2, Supporting Information). According to their descriptions during the follow-up visit, and the t-SNE analysis in Figure 5f also showed that the

dimensionality reduction space locations of subject Nos. 5, 8, 9, and 11 are at the area of the ill. These results demonstrate preliminarily the effectiveness of the MAS for the recovery assessment. And we anticipate that with more patient's data being gathered for training, the MAS's prediction and assessment accuracy can be improved further, and therefore, more specific symptoms can be classified further.

3. Discussion

In summary, we demonstrated an AMSA capable of real-time monitoring the personal plantar pressure. By combining with the machine-learning approach, as well as the data collecting/transmitting circuits and APP, it can recognize the common personal activities. More importantly, clinical experiments on LDD patients demonstrate that, the MAS system shows a diagnosis assisting ability, achieving a prediction accuracy rate of 100% after being trained with 125 individual samples. Furthermore, it shows an excellent recovery assessment preliminarily, on the postoperative patients, corresponded well with the doctors' diagnosis results.

Notably, LDD contains several symptoms, as well as various severity degrees. According to our analysis, presented in Figure 4c,d, more eigenvalues need be investigated to further enhance the present machine-learning method, and eventually classify various symptoms and severity degrees. As the training samples becomes more, and the medical cloud database builds up, these concepts may therefore form a starting point for AI and remote medical services. Since personal plantar pressure is also indicative of other diseases, such as diabetes and fasciitis, the system can be extended to other medical aspects, showing a broad impact in biomedical engineering.

4. Experimental Section

Fabrication of AMSA: The FPCB was designed to the shape of an insole by Altium Designer according to the distribution of plantar pressure. The printed copper square (1cm × 1cm) areas serve as the anode and the rectangle areas around were the cathode, which constitutes the input electrode of AMSA (Figure S1, Supporting Information). Silver-coated PVDF films were tailored into square shapes with a size of 1 cm × 1 cm. A CO_2 laser cutter defined pieces of double-side tapes (0.95 cm × 0.95 cm) and single-side tapes (1.2 cm × 1.2 cm). The double-side tapes stick the PVDF film and anode together. The single-sided tape covered the PVDF film that connects its top surface to the cathode (Figure S1c, Supporting Information). The double-sided tapes were smaller than PVDF films and single-side tapes in order not to cause a short circuit. 17 sensors made up an active-matrix to sense the plantar pressure. The signal layer was full of ground electrodes as shield in order to avoid the noise disturbance. In the end, the FPCB was encapsulated with leather (sheep skin) to improve its robustness. The manufacturing information of FPCB is summarized in Table S3, Supporting Information.

Design of the Data Acquisition Circuit: The PCB achieves the function of signal's amplification, data acquisition, and data transmission. Pressure modulated current signal inputs to the amplifier and then the amplified voltage outputs to the main chip for sampling. The main chip samples the voltage of 17 sensors in turn through an analog switch because of the limited sampling channel. The sampling time was 8 µs and the sampling conversion mode was the repeat-sequence-of-channels mode. Then the data were transmitted to Bluetooth chip through serial communication with a baud rate 115 200. The low-power Bluetooth retransmits the data to a cell phone operating at notifying mode with the interval of 100 ms. The manufacturing and component information is summarized in Table S4, Supporting Information.

The PCB was designed by Altium Designer 2016. The program of main chip was written by assembly language to improve the execution efficiency. The Bluetooth program was exploited by C language. The data were transmitted between main chip and Bluetooth chip through serial communication. Terminal app operating on Android 10 was exploited by JAVA with visual studio platform. It can display the plantar pressure distribution with map graph or every single sensor's output in real-time. The received data can be stored at storage temporarily or sent to computer or server for another process. In order to save the memory, the form of the data was stored as ".txt".

Data Collection: A pair of insoles collect people's pressure data and transmit to cell phones through Bluetooth in real-time after the PCB was powered on. All the samples were collected from one person (male, 180 cm height, 70 kg weight). Every kind of motion data set includes 45 samples totally 225 samples divided into 190 samples (38 samples of each motion) for model training and 35 samples (7 samples of each motion) for prediction at random. For each sample, the participants repeat the motion lasting for 1 min. The frequency of half-squat, squat, jump, walk, and jog was ≈0.25, ≈0.2, ≈0.2, 2, and 3 Hz, respectively, and the frequency was 1 and 1.5 Hz for single step when walking and jogging, respectively.

For LDD distinction, a total 83 of clinic samples were acquired including 62 samples for model training, 10 samples for prediction, and 11 recovery samples. 73 samples of normal people were acquired to divide 63 samples for model training and 10 samples for prediction. 53 patients (19 males, 34 females, weight ranging from 51 to 91 kg) and 42 normal people (30 males, 12 females, weight ranging from 48 to 83 kg) were selected at random to collect plantar pressure by MAS. The information of patients, recovery people, and normal people can be found in Tables S1 and S2, Supporting Information. Patients and normal people walk around the ward lobby or laboratory corridor for a continuous walking lasting around 1 min and a half, and then send the data to computer to process and analysis.

This was a cross-sectional prospective study that was approved by the Ethics Committee of Peking University Third Hospital (No.M2021091). All the studies have gotten the approval from the participants. The demo of data collection procedure can be found in Movie S1, Supporting Information.

Data Preparation for Machine-Learning: After sampling, 17 sensors make up a 17 dimensions matrix. Then, the average and variance values were calculated as eigenvalues of every dimension. After the eigenvalue extraction, the matrix was normalized between 0 to 1.

The Eigenvalues Choosing Principle: On the one hand, the eigenvalue should be relevant to the study and the importance of eigenvalue choosing was to eliminate irrelevant and redundant features, for example, age and gender for the plantar pressure study. On the other hand, the eigenvalue can't be selected infinitely which should consider the computational capabilities. As the system output a multidimensional data, the computational power consumed will grow exponentially if choose more eigenvalues.

t-SNE Analysis: 34 dimensions of data were dimensionality reduced to 2 dimensions to exhibit the relationship of multidimensional data.

The Experience Conditions: The output performance of sensors (Figure 2) was tested through an electrometer KEITHLEY 6517 (Figure S5, Supporting Information). The data and data graph were processed by using Origin 2018. The program of machine-learning algorithm including model training and prediction runs on the MATLAB 2018a.

Supporting Information

Supporting Information is available from the Wiley Online Library or from the author.

Acknowledgements

D.L., D.Z., and Z.S. contributed equally to this work. This work was supported by the National Key R&D Project from Minister of Science and Technology (Grant No. 2016YFA0202704), National Natural Science Foundation of China (Grant Nos. 51432005, and 5151101243), and Youth Innovation Promotion Association, CAS. All procedures in the tests in healthy individuals and LDD patients were in accordance with the experimental protocol approved by the Committee on the Use of Humans as Experimental Subjects of the Peking University Third Hospital, Department of Orthopaedics (No. M2021091). The participants gave informed consent.

Conflict of Interest

The authors declare no conflict of interest.

Data Availability Statement

The data that support the findings of this study are available from the corresponding author upon reasonable request.

Keywords

active-matrix sensing array, intelligence diagnosis, machine learning, motion classification, piezoelectric sensors, recovery assessments

Received: December 20, 2021
Published online:

[1] K. P. Botwin, R. D. Gruber, *Phys. Med. Rehabil. Clin. N. Am.* **2003**, *14*, 1.
[2] C. Reinshagen, N. Redjal, M. Molcanyi, B. Rieger, *EBioMedicine* **2015**, *2*, 1005.
[3] J. Hartvigsen, M. J. Hancock, A. Kongsted, Q. Louw, M. L. Ferreira, S. Genevay, D. Hoy, J. Karppinen, G. Pransky, J. Sieper, R. J. Smeets, M. Underwood, *Lancet* **2018**, *391*, 2356.
[4] D. M. Coombs, G. C. Machado, B. Richards, R. Wilson, C. G. Maher, *Lancet Reg. Health West Pac.* **2021**, *7*, 100089.
[5] R. A. Richard, S. K. Mirza, B. I. Martin, W. Kreuter, D. C. Goodman, J. G. Jarvik, *JAMA, J. Am. Med. Assoc.* **2011**, *306*, 1259.
[6] G. D. Schroeder, M. F. Kurd, A. R. Vaccaro, *J. Am. Acad. Orthop. Surg.* **2016**, *24*, 843.
[7] C. Weber, C. Giannadakis, V. Rao, A. S. Jakola, U. Nerland, Ø. P. Nygaard, T. K. Solberg, S. Gulati, O. Solheim, *SPINE* **2016**, *41*, E78.
[8] H. J. Andrew, C. C. Tomkins, *JAMA, J. Am. Med. Assoc.* **2010**, *303*, 71.
[9] N. C. Papadakis, D. G. Christakis, G. N. Tzagarakis, G. I. Chlouverakis, N. A. Kampanis, K. N. Stergiopoulos, P. G. Katonis, *Physiol. Meas.* **2009**, *30*, 1171.
[10] M. N. Stienen, A. L. Ho, V. E. Staartjes, N. Maldaner, A. Veeravagu, A. Desai, O. P. Gautschi, D. Bellut, L. Regli, J. K. Ratliff, J. Park, *Spine J.* **2019**, *19*, 1276.
[11] C. Uden, M. P. Besser, *BMC Musculoskeletal Disord.* **2004**, *5*, 13.
[12] J. Sun, Y. C. Liu, S. H. Yan, S. S. Wang, D. K. Lester, J. Z. Zeng, J. Miao, K. Zhang, *Orthop. Surg.* **2018**, *10*, 32.
[13] M. N. Stienen, P. G. Rezaii, A. L. Ho, A. Veeravagu, C. C. Zygourakis, C. T. Lane, J. Park, J. K. Ratliff, A. M. Desai, *Sci. Rep.* **2020**, *10*, 4939.
[14] M. Lord, D. P. Reynolds, J. R. Hughes, *J. Biomed. Eng.* **1986**, *8*, 283.
[15] J. Krzaczek, G. Mcnelis, J. Eisenhardt, *Bioengineering Conference*, IEEE, Durham, NH, USA **1988**.
[16] J. A. Ramirez-Bautista, S. L. Chaparro, A. H. Zavala, J. A. Huerta, *Biocybern. Biomed. Eng.* **2018**, *38*, 342.
[17] B. Eskofier, S. I. Lee, M. Baron, A. Simon, C. F. Martindale, H. Gabner, J. Kluchen, *Appl. Sci.* **2017**, *7*, 986.
[18] S. I. Lee, E. Park, A. Huang, B. Mortazavi, J. H. Garst, N. Jahanforouz, M. Espinal, T. Siero, S. Pollack, M. Afridi, M. Daneshvar, S. Ghias, D. C. Lu, M. Sarrafzadeh, *Med. Eng. Phys.* **2016**, *38*, 442.
[19] M. Peulic, M. Jokovic, T. Šušteršič, A. Peulic, *Comput. Math. Methods Med.* **2020**, *3*, 6320126.
[20] A. H. Razak, M. Peulic, M. Sustersic, *Sensors (Basel)* **2012**, *12*, 9884.
[21] A. Rozumalski, M. H. Schwartz, *Gait Posture* **2011**, *33*, 730.
[22] H. H. M. Battesha, R. Elhak, *Int. J. Ther. Rehabil.* **2020**, *27*, https://doi.org/10.12968/ijtr.2019.0026.
[23] M. Saito, K. Nakajima, C. Takano, Y. Ohta, C. Sugimoto, R. Ezoe, K. Sasaki, H. Hosaka, T. Ifukube, S. Ino, K. Yamashita, *Med. Eng. Phys.* **2011**, *33*, 638.
[24] A. Healy, P. B. Walker, R. Naemi, N. Chockalingam, *Foot* **2012**, *22*, 35.
[25] R. A. Lakho, Z. Yi-Fan, J. J. Hua, H. C. Yu, Z. A. Abro, *Text. Res. J.* **2019**, *89*, 3433.
[26] A. Ciniglio, A. Guiotto, F. Spolaor, Z. Sawacha, *Sensors* **2021**, *21*, 1450.
[27] C. J. Burges, *Data Min. Knowl. Discov.* **1998**, *2*, 121.
[28] G. Yamankurt, E. J. Berns, A. Xue, A. Lee, C. A. Mirkin, *Nat. Biomed. Eng.* **2019**, *3*, 318.
[29] K. Lee, X. Ni, J. Y. Lee, H. Arafa, J. A. Rogers, *Nat. Biomed. Eng.* **2020**, *4*, 148.
[30] C. Li, D. Liu, C. Xu, T. Wang, Z. L. Wang, *Nat. Commun.* **2021**, *12*, 2950.
[31] C. Zhang, S. Liu, X. Huang, W. Guo, Y. Li, H. Wu, *Nano Energy* **2019**, *05*, 046.
[32] Z. Li, W. Guo, Y. Huang, K. Zhu, H. Yi, H. Wu, *Carbon* **2020**, *164*, 164.
[33] Z. Zhou, K. Chen, X. Li, S. Zhang, J. Chen, J. Yang, *Nat. Electron.* **2020**, *3*, 571.
[34] K. Meng, S. Zhao, Y. Zhou, Y. Wu, S. Zhang, H. Qiang, W. Xue, Z. Zhou, W. Fan, X. Tan, J. Yang, J. Chen, *Matter* **2020**, *2*, 896.
[35] Z. L. Wang, *Science* **2006**, *312*, 242.
[36] C. Deng, W. Tang, L. Liu, B. Chen, M. Li, Z. L. Wang, *Adv. Funct. Mater.* **2018**, *28*, 1801606.
[37] A. V. Shirinov, W. K. Schomburg, *Sens. Actuators, A* **2008**, *142*, 48.
[38] A. Gisbrecht, A. Schulz, B. Hammer, *Neurocomputing* **2015**, *147*, 71.
[39] A. Patle, D. S. Chouhan, *International Conference on Advances in Technology & Engineering*, IEEE, Mumbai, India **2013**.
[40] V. Cherkassky, Y. Q. Ma, *Neural Networks* **2004**, *17*, 113.
[41] B. Jing, X. Zhang, Y. Guo, *Different inertia weight PSO algorithm optimizing SVM kernel parameters applied in a speech recognition system*, IEEE, Changchun, China **2009**.
[42] C. T. Jeremy, P. B. Pynsent, *SPINE* **2000**, *25*, 2940.